

Contents

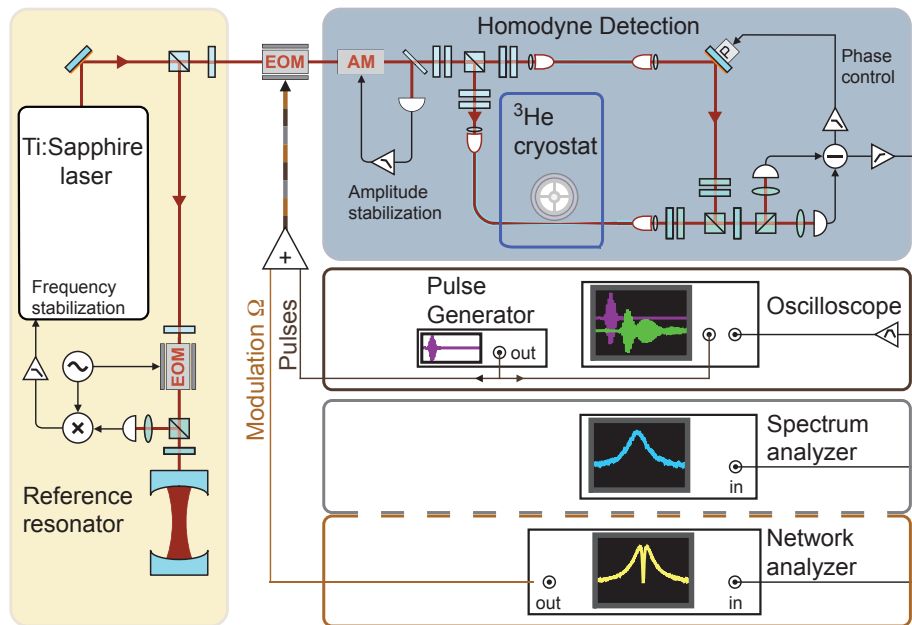
1	Experimental details	2
1.1	Experimental setup	2
1.2	Influence of guided acoustic wave Brillouin scattering	3
1.3	Time-domain response	5
2	Optimized spoke anchored toroidal resonator	6
2.1	Sample design	6
2.2	Sample fabrication	8
2.3	Sample characterization	9
3	Modeling of optomechanical interaction	11
3.1	Conservative dynamics	11
3.2	Quantum Langevin equations	12
3.3	Linearized model	14
3.4	Homodyne detection	15
3.5	Calculation of noise covariances	16
3.6	Coherent dynamics of the system	17
3.7	Analysis of the coherent response	17
3.8	Extraction of the decoherence rate	19
3.9	Error analysis	19

1 Experimental details

1.1 Experimental setup

Figure 1 shows a schematic of the employed experimental setup. At the heart of the optical setup is a Ti:Sapphire laser (Sirah Matisse TX) operating at a wavelength around 780 nm. The laser exhibits quantum limited amplitude and phase noise at Fourier frequencies relevant for this experiment. During the experiments the laser is locked to an external reference cavity such that drifts of the laser detuning Δ can be neglected during the acquisition time.

The sample itself resides in a helium-3 exchange gas cryostat (Oxford Instruments Heliox TL) that is used for cryogenic pre-cooling of the mechanical mode to low temperatures. Since the toroids are situated directly above the surface of the liquified helium-3, the achievable temperature is directly linked to the vapor pressure curve of helium-3. As the toroidal microstructures are thermally very well isolated from the substrate, one relies on cooling via the helium-3 exchange gas. As a consequence, cryostat temperature setpoints of at least 650 mK (corresponding to pressures larger than ≈ 0.15 mbar) are favorable. Coupling of light into the toroid is achieved via a tapered optical fiber that is approached using piezo positioners, which are compatible with low temperature operation (Attocube GmbH). The fiber ends are guided through and out of the cryostat and



Supplementary Figure 1: **Setup.** See text for details.

constitute one arm of the interferometer that is part of the balanced homodyne detection scheme. The length of one of the ca. 8 m long arms is servo-locked using a movable mirror to cancel the DC-component of the interferometer's signal. This setting allows a shot-noise limited read-out of the phase noise imprinted onto the transmitted laser field. The laser passes an electro-optical modulator that allows to create sidebands around the laser frequency. Last, the laser power is stabilized actively in absolute terms at the input of the experiment to ensure operation at a constant light intensity.

The three colored building blocks highlighted in Figure 1 depict the three different measurements that are routinely performed one after the other.

- *Coherent response.* A network analyzer sweeps the upper modulation sideband over the optical resonance and demodulates the corresponding (coherent) signal (cf. section 3.6).
- *Noise spectrum.* Connecting only an electronic spectrum analyzer gives access to the incoherent noise spectrum (cf. section 3.5).
- *Time domain response.* Sending a pulsed stimulus from an arbitrary waveform generator to the EOM which modulates the coupling laser gives access to the dynamic time domain response of the optomechanical system (cf. section 1.3).

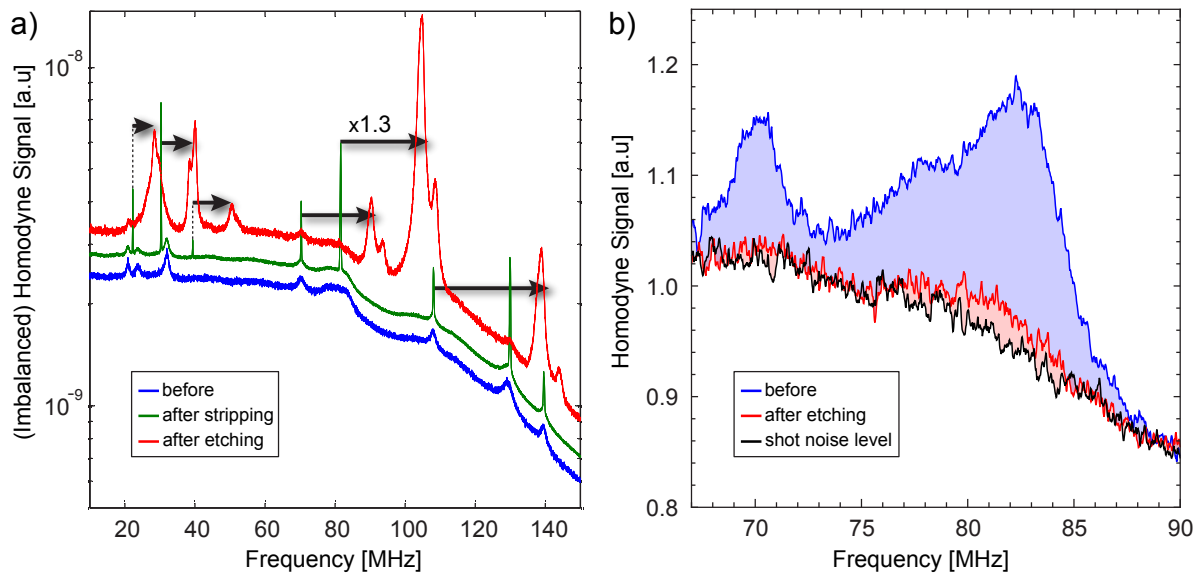
1.2 Influence of guided acoustic wave Brillouin scattering

A crucial prerequisite for optomechanical measurements in the quantum regime is the use of a quantum limited laser source. From the point of view of quantum manipulations, added noise in the coupling beam corresponds to an improper state preparation, the optical beam being in a statistical mixture of pure quantum states. In the weak coupling limit $\Omega_c \ll \kappa$, where the optical field acts as an effective bath, these extra fluctuations correspond to an increased temperature of the bath and prevents cooling close to the quantum ground state [1, 2, 3]. In addition, classical laser noise driving the optomechanical system can lead to ambiguous signatures such as squashing in the noise spectra, as reported previously [4]. We have verified in our previous work [5], that the employed laser source is quantum limited.

However, as is well known from fiber-based quantum optics experiments [6], optical fibers can give rise to classical phase noise, in the form of guided acoustic wave Brillouin scattering (GAWBS). This process involves thermally driven radial mechanical modes of the fiber, that also modulate the optical path length.

To investigate the presence of GAWBS we have recorded the noise spectrum from the homodyne detector when the fiber is retracted away from the optomechanical cavity in an

imbalanced Mach-Zehnder interferometer. Several classical peaks are observed on top of the shot-noise background (not corrected for the detector response)(Fig. 2). The width (i.e. damping) of the noise peaks was observed to narrow dramatically when the buffer was partly stripped off the fiber, clearly demonstrating the mechanical nature of the peaks. One of the peaks coincides with the mechanical resonance frequency of 78 MHz. However, the frequency of the dilatational fiber modes is proportional to the inverse fiber radius and can therefore be shifted by etching the fiber cladding in an HF solution. Immersing the fibers (without removing the acrylate buffer, which is permeable to HF) in a 40 % HF solution for 50 minutes reduced the cladding diameter from 125 μm to 95 μm . This increased the GAWBS mode frequencies of all fibers in the setup by $\approx 30\%$, shifting them



Supplementary Figure 2: **Engineering of the fiber GAWBS noise spectrum.** The figure shows a broadband background spectrum of the imbalanced homodyne signal where the GAWBS modes are visible. Blue, green and red trace are taken with unmodified, partly stripped buffer and (almost entirely) etched fiber respectively. As expected for guided dilatational acoustic waves of the optical fiber the frequencies are increased by a factor of about 1.3 for a thinned fiber of around 95 μm diameter (as compared to 125 μm before). Doublets in the red trace are due to slightly different final etching radii (difference is about 3 μm) of the different fibers in our setup (i.e., local oscillator fiber and the signal fiber). The difference in relative heights of the peaks is attributed to varying readout conditions, and as such only the peak's frequencies are of interest. The inset shows a zoom of the background for the final setup (i.e., etching reduced diameter fibers, balanced homodyne arm lengths) and illustrates the achieved improvements, i.e., the reduced contribution of GAWBS to the background at the mechanical resonance frequency.

away from the mechanical resonance frequency of the toroid (Fig. 2a).

The data shown in Fig. 2b have been taken under the same conditions as the lowest occupation run shown in Fig. 2 of the main manuscript. The residual noise at 78 MHz (due to small portions of fibers that have not been etched) is approximately a factor seven smaller than the initial peaks, corresponding to a noise level of approximately 2% of the shot-noise. This noise is generated along the fibers, both before and after the cavity. Special care was taken to minimize the length of unetched fiber before the cavity. The fact that an influence of the cavity detuning and coupling parameters on the transduction of these classical noise peaks into a measured signal is not discernible indicates that indeed most remaining noise originates from fiber after the cavity. Under this assumption, the independent noise of the GAWBS can be subtracted from the signal in order to estimate the decoherence rate and occupation. Figure 2c in the main text shows that the shape of the spectra, as predicted from independently measured parameters, is in excellent agreement with the data after subtraction, in which no signs of squashing are observed. Nonetheless, we have performed an additional analysis for the lowest-occupancy data under the assumption that half of the noise is generated before the cavity, which leads to deviations of the decoherence rate and occupation of 7% and 5%, respectively. This upper bound of the influence of GAWBS, corresponding to an uncertainty of 0.08 phonons, is included in the quoted errors (cf. section 3.9).

1.3 Time-domain response

In order to probe the coherent dynamics of the optomechanical system in the time domain, the strong pump beam is tuned to the red sideband, and an RF pulse, resonant with the mechanical oscillator, is sent to the EOM. The upper modulation sideband excites the strongly coupled system. The subsequent evolution of the transmitted signal is recorded using the homodyne detector and an oscilloscope.

An arbitrary signal generator (Agilent 33250A) is used to generate the RF pulses. The time dependent voltage $U(t)$ is a sine wave modulated by a Gaussian envelope:

$$U(t) = E(t) \sin(\Omega_{\text{mod}}t + \phi_0) \quad (\text{S1})$$

$$E(t) = U_0 e^{-\left(\frac{t-t_0}{\tau}\right)^2} \quad (\text{S2})$$

with a carrier frequency $\Omega_{\text{mod}} = 2\pi \cdot 77$ MHz and an envelope duration $\tau = 32$ ns (FWHM = 54 ns). A digital oscilloscope, synchronously triggered with the signal generator is used to record and average the homodyne response. The very small signal originating from the balanced detectors is amplified and filtered, around a frequency of 75 MHz, with a bandwidth of 100 MHz. For low excitation amplitude, averaging is necessary to extract the coherent response out of the incoherent thermal and quantum noises from the optomechanical system.

The modulation depth $\beta(t)$ corresponding to the instantaneous value of the slowly varying envelope is given by:

$$\beta(t) = \pi \frac{E(t)}{V_\pi}, \quad (\text{S3})$$

where $V_\pi = 154$ V is the voltage corresponding to a π phase shift of the beam in the EOM (NewFocus 4002). For a weak modulation depth ($\beta \ll 1$), a fraction $(\beta/2)^2$ of the optical carrier power P_c is scattered into each of the two first modulation sidebands. The total optical power in the upper sideband can hence be simply approximated by

$$P(t) \approx P_c \left(\pi \frac{E(t)}{2V_\pi} \right)^2 \quad (\text{S4})$$

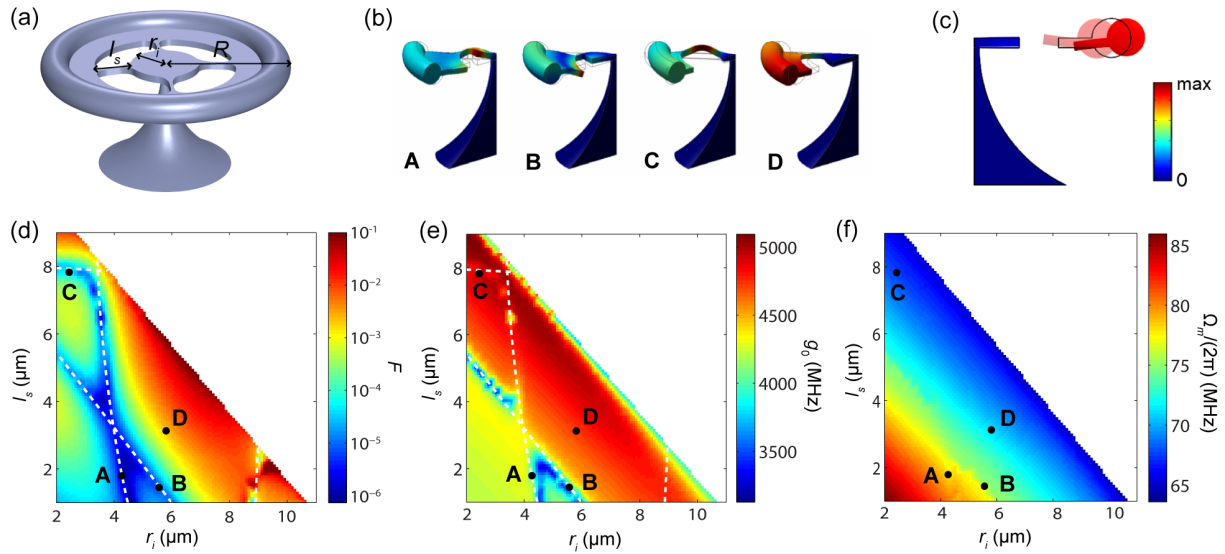
The total energy in the pulse can then be obtained by integrating the instantaneous power over the duration of the pulse. The average number of photons in one pulse is hence given by:

$$n \approx \frac{1}{\hbar\omega} \int_{-\infty}^{+\infty} P_c \left(\frac{\pi E(t)}{2V_\pi} \right)^2 dt = \frac{\pi^{5/2} \tau P_c}{4\sqrt{2} \hbar\omega} \left(\frac{U_0}{V_\pi} \right)^2 \quad (\text{S5})$$

2 Optimized spoke anchored toroidal resonator

2.1 Sample design

The optomechanical microresonators investigated in this work are specially designed toroidal microcavities, optimized to achieve large optomechanical coupling rates and small dissipation. Toroidal silica whispering gallery mode microresonators exhibit mechanical modes coupled to the optical modes through radiation pressure [7]. Of particular interest is the lowest order radial breathing mode (RBM), whose motion maximally modulates the optical cavity length. In the context of quantum-coherent coupling, it is important to simultaneously achieve large values of Ω_c/γ and Ω_c/κ , where $\Omega_c = 2g_0 |\bar{a}|$. The vacuum optomechanical coupling rate is given by $\frac{\omega}{R} \sqrt{\hbar/(2m_{\text{eff}}\Omega_m)}$, where R is the toroid radius, m_{eff} is the effective mass, and ω and Ω_m are the optical and mechanical resonance frequencies, respectively. For a given incident power, optical frequency, and environment temperature, and assuming the resolved sideband regime and the coupling laser being tuned to the lower mechanical sideband, one obtains $\Omega_c/\gamma \propto \left(R \Gamma_m \sqrt{\Omega_m m_{\text{eff}}/\kappa} \right)^{-1}$ and $\Omega_c/\kappa \propto \left(R \Omega_m^{3/2} \sqrt{m_{\text{eff}}\kappa} \right)^{-1}$. It is therefore obviously beneficial to reduce the sample dimensions to decrease R and m_{eff} . However, such miniaturization is generally accompanied by an increase of the mechanical frequency Ω_m , as well as an increase of Γ_m due to enhanced clamping losses. In microtoroids, both of these adverse effects can be countered



Supplementary Figure 3: **Sample optimization by finite element modeling.** See text for details.

in a design in which the toroid is suspended by spokes from the central pillar, as shown in Fig. 3a.

The introduction of spokes serves three purposes. First, they isolate the mechanical motion of the toroidal RBM from the pillar support, strongly reducing clamping losses [8]. Second, they reduce the mechanical mode volume and thereby the effective mass. Third, the effective spring constant is reduced, which lowers the mechanical resonance frequency. In practice, one needs to carefully consider the precise dimensions and positioning of the spokes, as these strongly affect both clamping losses Γ_{clamp} and g_0 . Figure 3b shows the displacement profile of the RBM of a spoke-supported toroid of radius $R = 15 \mu\text{m}$ for various combinations of spoke length and position, as simulated with a finite element method. The SiO_2 thickness is $1 \mu\text{m}$, the minor toroid radius is $2 \mu\text{m}$, the spoke width is 500 nm , the pillar diameter is $1 \mu\text{m}$, and the toroid is vertically offset from the middle SiO_2 disk by 400 nm . Since we are interested in the RBM only, it suffices to simulate $1/8$ portion of the microresonator while assuming symmetric boundary conditions on both of the two ‘cut’ planes. As can be seen from these examples, the mechanical mode profiles can change drastically depending on the spoke dimensions. Of the examples in Fig. 3b, only ‘D’ depicts a mode that is purely localized to the outer toroid, with purely radial displacement, as illustrated in the cross-section in Fig. 3c.

The origin of this wildly varying nature of the RBM is revealed in Fig. 3d, where the radius r_i of the inner disk (defining the spoke placement) and the spoke length l_s are

varied systematically. The colorscale depicts the parameter F , defined as

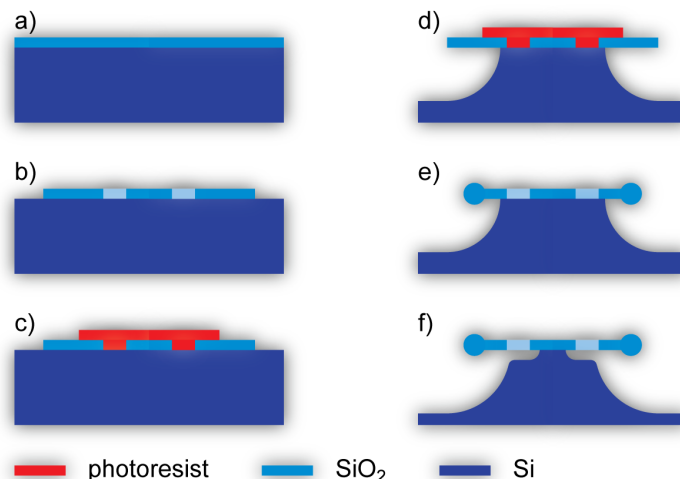
$$F = \frac{2\pi E_{\text{mech}}}{c\rho\Omega_m^2 \int_{A_p} |\Delta z(\mathbf{x})|^2 dA}. \quad (\text{S6})$$

Here, E_{mech} is the total mechanical energy in the mode, c the speed of sound in silica, ρ the density of silica, and $\Delta z(\mathbf{x})$ the out-of-plane displacement amplitude, with the integration extending over the area A_p of the interface between the pillar and the silica disk. F is proportional to the expected value of $\Gamma_{\text{clamp}}^{-1}$, when the clamping area A_p is considered as a membrane radiating energy with a power $P = c\rho\Omega_m^2 \int_{A_p} |\Delta z(\mathbf{x})|^2 dA$ [8]. A previous study has experimentally found a correspondence of $F \approx (3\Gamma_{\text{clamp}}/(2\pi))^{-1}$ for larger toroids. As can be seen from the figure, the expected clamping losses vary strongly with spoke dimensions, ranging from 10^1 to 10^6 Hz. Most notably, several lines can be identified in this parameter space where clamping losses are large (indicated by the dashed lines). For parameter combinations along each of these lines, the RBM frequency approaches that of another mechanical mode of the structure. As a result, the two modes exhibit an anticrossing, with the hybridized modes showing a character of both uncoupled modes. This is the case for examples ‘A’, ‘B’, and ‘C’ in Fig. 3b, which show the RBM hybridized with a flexural mode of the inner SiO₂ disk, the outermost SiO₂ membrane, and the spoke itself, respectively. In the vicinity of these anticrossings, the vertical displacement at the pillar, and as such the radiation into the substrate F^{-1} , are strongly enhanced. To achieve a design that exhibits small clamping losses, it is therefore crucial to avoid these parameter regions, as is the case for mode ‘D’ in Fig. 3b.

The aforementioned anticrossings affect the coupling rate g_0 as well, albeit to a lesser degree. Fig. 3e shows g_0 , calculated as in [9], assuming the optical mode is localized at the edge of the toroid with negligible transverse size. At the anticrossings, g_0 is reduced (i.e., the effective mass is increased), as a significant part of the mode’s energy is in that case associated with displacements that do not modulate the cavity length. Away from the anticrossings, however, the RBM mode is localized exclusively in the toroid and outermost part of the membrane, well isolated from the inner disk and pillar support. As a result, m_{eff} is nearly identical to the physical mass of this volume. It is therefore important to minimize the volume of the outermost membrane, i.e., the distance between the spokes and the toroid. As can be seen in Fig. 3f, this simultaneously allows to reach the smallest possible resonance frequency. In practice, the laser reflow process used to form the toroid poses a lower limit on the remaining distance between spokes and toroid.

2.2 Sample fabrication

To fabricate the spoke-anchored microresonators, we use a combination of optical lithography and dry etching techniques outlined in Fig. 4. In a first step (b), a disk including the spokes is transferred in a 1 μm thick film of thermal oxide on a Si wafer (a), through



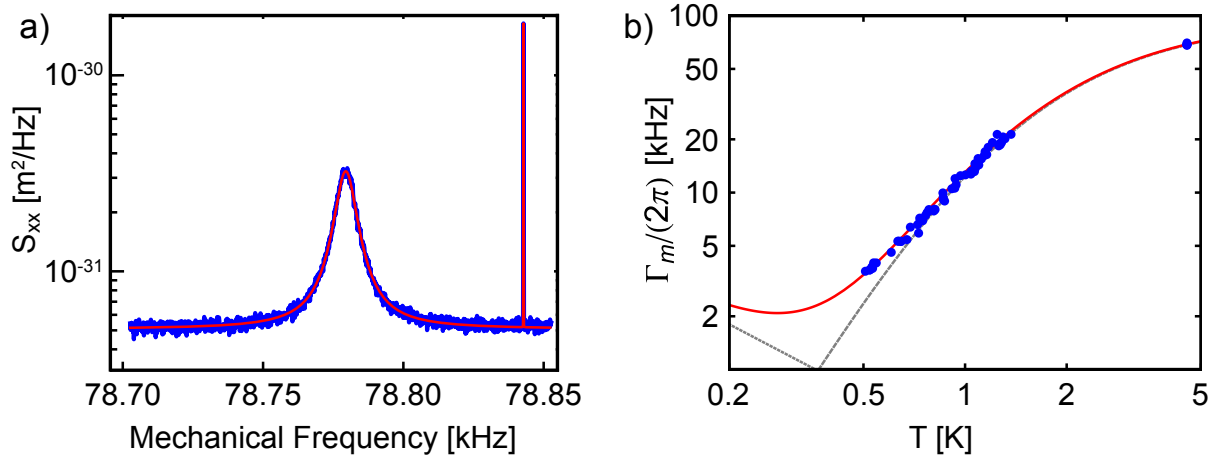
Supplementary Figure 4: **Sample fabrication.** See text for details.

optical lithography followed by reactive ion etching of the SiO₂. In a second photolithography step (c), smaller disks of photoresist are defined that cover the center of the SiO₂ disks, including the spokes. These serve to protect the exposed Si surface between the spokes during the subsequent isotropic XeF₂ etch (d) of the Si substrate. Care is taken to stop the etch shortly before it reaches the apertures in the SiO₂ disk. After removing the protective photoresist disks, a laser reflow of the underetched disk is performed (e), forming the silica toroid. Finally (f), a second XeF₂ etch releases the toroid and reduces the pillar diameter, typically to a value smaller than 1 μm .

2.3 Sample characterization

The vacuum optomechanical coupling rate g_0 is measured at room temperature in a vacuum chamber. Therefore, the mechanical motion is read out using an external cavity tunable diode laser at 1550 nm, that is locked to a cavity resonance. In order to avoid any radiation pressure effects we perform these measurements at very low laser power (typically around 100 nW). The transmitted light is amplified by a low noise erbium-doped fiber amplifier and sent onto a photodetector. For absolute calibration of the mechanical spectrum registered by an electronic spectrum analyzer, we use a phase-modulation technique [10]. We extract a vacuum optomechanical coupling rate of $g_0 = 1700$ Hz for a wavelength of 1550 nm (i.e. $g_0 = 3400$ Hz at 780 nm).

The mechanical linewidth measured at room temperature (8.1 kHz) was found to be higher than expected from the calculated F-parameter (cf. section 2.1). However, performing the same measurements in the cryostat (cf. Fig. 5b), a linewidth as low as 3.6 kHz was found on the same microresonator, indicating that a loss mechanism other than clamping losses must dominate at room temperature. Since there losses due to two level



Supplementary Figure 5: **Sample characterization.** a) shows a calibrated mechanical noise spectrum for the resonator used throughout the manuscript (except the last panel of Fig. 4 of the main manuscript), which was measured at room temperature in vacuum. The fit (red line) was used to extract a vacuum optomechanical coupling rate of 3400 Hz at 780 nm. b) mechanical damping of this toroid vs. cryostat temperature. The red line is a fit according to the TLS model presented in [11, 5], the grey lines represent the contributions from resonant (dotted) and relaxational (dashed) processes. The fit yields a negligible contribution of clamping losses.

fluctuators (TLS, [11, 12]) have been found to be significantly lower (linewidths below 4 kHz have been measured at room temperature for conventional toroids of similar frequency), we believe that the dominating loss mechanism is thermo-elastic damping (TED) [13]. At low temperatures, where TED is strongly reduced, the main loss mechanism is coupling to TLS. Figure 5b shows the measured temperature dependence of the mechanical linewidth at low temperature, obtained with the laser (with 100 nW power) resonant with the, in this case, strongly overcoupled optical resonance to avoid dynamical back-action. The variation of Γ_m with temperature can be fitted using a model for the TLS losses [11, 5]. It is found that this mechanism dominates the total losses for all reachable cryogenic temperatures. This means that it is not possible to retrieve an accurate estimation of the temperature-independent contribution Γ_{clamp} . We can however conclude that it must be at least smaller than 2 kHz for this sample. This shows that in our optimized spoke-supported design, we have successfully mitigated the clamping losses to the level where they are insignificant compared to intrinsic dissipation.

3 Modeling of optomechanical interaction

This section summarizes the theoretical model which was used to extract all entities of interest from our data. Figure 6 shows the parameters and variables of the model, and their mutual connections.

3.1 Conservative dynamics

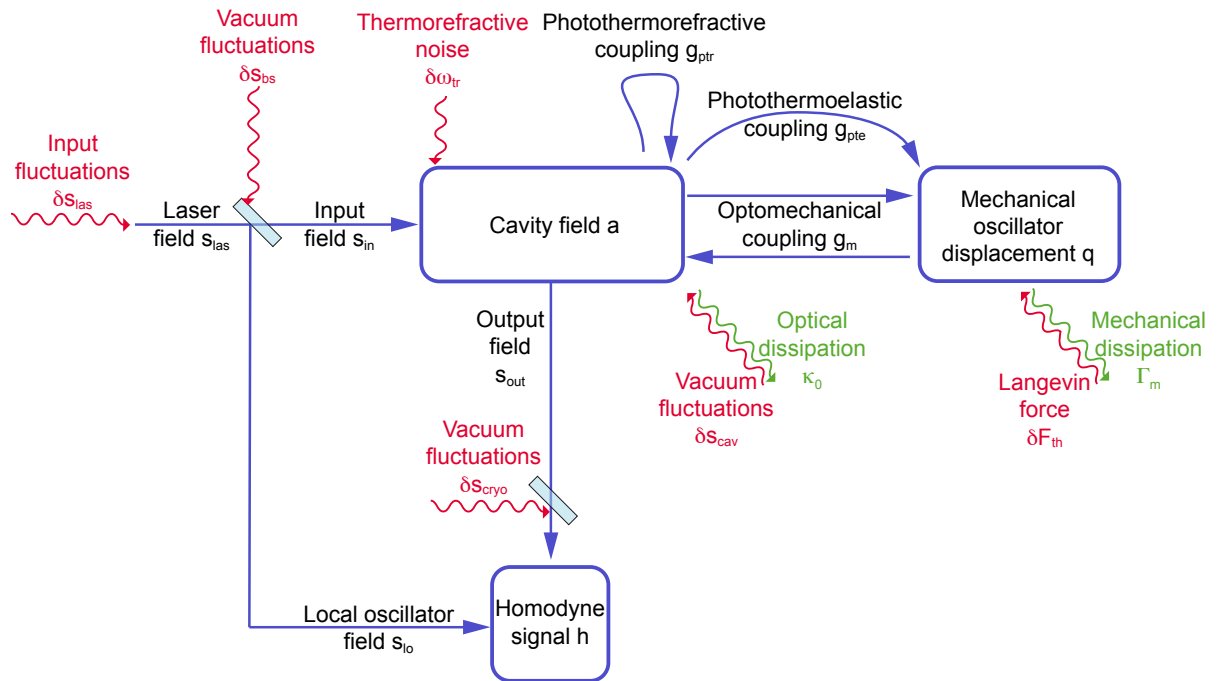
The conservative dynamics of an optomechanical system are described by the Hamiltonian [14]

$$H = \frac{1}{4}\hbar\Omega_m (q^2 + p^2) + \hbar\omega_c \left(a^\dagger a + \frac{1}{2} \right) + \hbar g_0 q a^\dagger a, \quad (\text{S7})$$

where mechanical quadrature operators q and p are related to the corresponding mechanical ladder operators b and b^\dagger via

$$q = b + b^\dagger \quad (\text{S8})$$

$$p = (b - b^\dagger)/i. \quad (\text{S9})$$



Supplementary Figure 6: **Theoretical model used.** See text for details.

With these definitions $[q, p] = 2i$, and the actual mechanical displacement and momentum are given by $x' = x_{\text{zpm}}q$ and $p' = \hbar p/2x_{\text{zpm}}$ with the amplitude of the zero-point motion

$$x_{\text{zpm}} = \sqrt{\frac{\hbar}{2m_{\text{eff}}\Omega_{\text{m}}}}. \quad (\text{S10})$$

The vacuum optomechanical coupling rate g_0 quantifies the strength of the optomechanical interaction and is given by $g_0 = Gx_{\text{zpm}}$ with $G = \partial\omega_{\text{c}}/\partial x$.

3.2 Quantum Langevin equations

The Hamiltonian (S7) determines the conservative evolution of the optomechanical degrees of freedom. Optical and mechanical dissipation, and the corresponding fluctuations, can be taken into account by introducing the mechanical dissipation rate Γ_{m} and the optical dissipation rate $\kappa = \kappa_0 + \kappa_{\text{ex}}$ (where κ_{ex} represents losses to the coupling waveguide and κ_0 all other optical losses) as well as the optical noise terms δs_{in} , δs_{cav} and the thermal Langevin force, which we express as a rate δf_{th} by writing the physical force in momentum units of $\hbar/2x_{\text{zpm}}$. This leads to the well-known Langevin equations of cavity optomechanics [15, 16, 17]

$$\dot{a}(t) = \left(i\Delta - \frac{\kappa}{2}\right)a(t) - ig_0q(t)a(t) + \sqrt{\kappa_{\text{ex}}}(\bar{s}_{\text{in}} + \delta s_{\text{in}}(t)) + \sqrt{\kappa_0}\delta s_{\text{cav}}(t) \quad (\text{S11})$$

$$\dot{q}(t) = \Omega_{\text{m}}p(t) \quad (\text{S12})$$

$$\dot{p}(t) = -\Omega_{\text{m}}q(t) - 2g_0a^\dagger(t)a(t) - \Gamma_{\text{m}}p(t) + \delta f_{\text{th}}(t), \quad (\text{S13})$$

where the convention $\Delta = \omega_{\text{l}} - \omega_{\text{c}}$ was used to denote the detuning of the laser (angular) frequency ω_{l} from the bare cavity resonance frequency ω_{c} , and a is expressed in a frame rotating at ω_{l} .

In order to accurately model the response of the optomechanical system over a wide range of parameters (detuning, Fourier frequency, optical and mechanical excitation) for a single set of parameters, we have refined this generic model by including other effects which are known to be inherent to most optical microcavities, and are discussed in the following.

Photothermoelastic backaction. Thermoelastic forces driven by temperature gradients induced by light absorption can induce mechanical displacements. The starting point to model these displacements are the coupled equations of motion known from the standard theory of thermoelasticity [13]

$$\mu \vec{\nabla}^2 \vec{u} + (\lambda + \mu) \vec{\nabla}(\vec{\nabla} \cdot \vec{u}) + \vec{f} = (3\lambda + 2\mu)\alpha \vec{\nabla}\theta + \rho \ddot{\vec{u}} \quad (\text{S14})$$

$$k_{\text{t}} \vec{\nabla}^2 \theta - c_{\text{t}} \rho \dot{\theta} = (3\lambda + 2\mu)\alpha T_0(\vec{\nabla} \cdot \dot{\vec{u}}) - v \kappa_{\text{abs}} a^\dagger a. \quad (\text{S15})$$

These equations connect the displacement field $\vec{u}(\vec{r}, t)$ and the temperature elevation $\theta(\vec{r}, t)$ above the mean temperature T_0 . Here, λ and μ are the Lamé parameters, α the

thermal expansion coefficient, ρ the mass density, \vec{f} a body force (e.g. due to radiation pressure), k_t the thermal conductivity, κ_{abs} the photon absorption rate, c_t the heat capacity, and the function $v(\vec{r})$ describes the spatial distribution of the light absorption. Evidently, a thermoelastic body force

$$\vec{f}_{\text{te}}(\vec{r}, t) = -(3\lambda + 2\mu)\alpha\vec{\nabla}\theta(\vec{r}, t) \quad (\text{S16})$$

acts on the mechanical modes of the structure when a temperature gradient $\vec{\nabla}\theta(\vec{r}, t)$ is present. In the scalar representation of the mechanical dynamics, we therefore have to add a thermoelastic force $f_{\text{te}}(t)$ proportional to the material parameters λ , μ and α , as well as an overlap integral of the mechanical mode's displacement pattern and the temperature gradient $\vec{\nabla}\theta(\vec{r}, t)$. Assuming that the temperature gradients are predominantly driven by the absorption of laser light in the resonator, one can express the scalar photothermoelastic force as

$$f_{\text{pte}}(t) = \chi_{\text{pte}}(t) * \kappa_{\text{abs}}a^\dagger(t)a(t), \quad (\text{S17})$$

where we have absorbed the spatial overlap integrals between the mechanical and (the gradient of) the thermal modes, as well as the thermal modes and the spatial pattern of light absorption into the magnitude of the function $\chi_{\text{pte}}(t)$. The temporal dynamics of the adjustment of the relevant temperature gradients to a changing amount of light absorption is represented by the time-dependence of $\chi_{\text{pte}}(t)$ (“*” denotes a convolution). Note that while this formulation accounts for the quantum fluctuations of the intracavity field $a(t)$, the statistical nature of photon absorption events is neglected. This is justified considering that the quantum fluctuations of optical heat deposition (“photothermoelastic shot noise”) have a much smaller effect on the mechanical mode than the direct fluctuations of the radiation pressure term $2g_0 a^\dagger a$.

Dynamic photothermorefractive frequency shift. A temperature elevation $\theta(\vec{r}, t)$ within the optical mode volume furthermore changes the refractive index, and therefore the optical resonance frequency. In analogy to the description in the previous section, we are using a simple scalar description of the form

$$\Delta\omega_{\text{ptr}}(t) = \chi_{\text{ptr}}(t) * \kappa_{\text{abs}}a^\dagger(t)a(t) \quad (\text{S18})$$

for this frequency shift, where the response function $\chi_{\text{ptr}}(t)$ accommodates spatial overlap integrals of the light absorption pattern $v(\vec{r})$ and the thermal modes as well as the temporal dynamics of the latter, and, in addition, the spatial sampling of the induced refractive index changes

$$\Delta n(\vec{r}, t) = \frac{dn}{dT}\theta(\vec{r}, t) \quad (\text{S19})$$

by the optical mode.

Thermorefractive noise. The local temperature elevation $\theta(\vec{r}, t)$ also undergoes thermal fluctuations—independent of the presence of light. Within a volume V , they amount to squared fluctuations of [18]

$$\langle \theta(\vec{r}, t)^2 \rangle_V = \frac{k_B T_0^2}{c_p \rho V}. \quad (\text{S20})$$

The spatial distribution of these fluctuations can be calculated using a Langevin ansatz [19], by adding a fluctuational source term to the heat diffusion equation (S15). Predominantly via the thermorefractive effect ($dn/dT \neq 0$), the resulting temperature fluctuations again induce resonance frequency fluctuations $\delta\omega_{\text{tr}}(t)$. Its temporal correlation function (or equivalently, power spectral density) have been estimated for simple whispering-gallery mode resonator geometries [20, 21, 22].

Taking these additional three effects into account, the equations of motion can be written as

$$\begin{aligned} \dot{a}(t) = & \left(i(\Delta - \Delta\omega_{\text{ptr}}(t) - \delta\omega_{\text{tr}}(t)) - \frac{\kappa}{2} \right) a(t) - ig_0 q(t) a(t) + \\ & + \sqrt{\kappa_{\text{ex}}}(\bar{s}_{\text{in}} + \delta s_{\text{in}}(t)) + \sqrt{\kappa_0} \delta s_{\text{cav}}(t) \end{aligned} \quad (\text{S21})$$

$$\dot{q}(t) = \Omega_m p(t) \quad (\text{S22})$$

$$\dot{p}(t) = -\Omega_m q(t) - 2g_0 a^\dagger(t) a(t) - \Gamma_m p(t) + \delta f_{\text{th}}(t) + f_{\text{pte}}(t). \quad (\text{S23})$$

3.3 Linearized model

A large coherent field sent to the optomechanical system induces a relatively large classical intracavity field \bar{a} , and induces a displacement of the mechanical mode by \bar{q} . If the system is stable around this steady-state, the dynamics of the small fluctuations around this equilibrium are described by a set of equations obtained via the substitution $a(t) = \bar{a} + \delta a(t)$ and $q(t) = \bar{q} + \delta q(t)$, and retaining only first-order terms in the fluctuations. This yields

$$\begin{aligned} \dot{\delta a}(t) = & \left(+i\bar{\Delta} - \frac{\kappa}{2} \right) \delta a(t) - i\kappa_{\text{abs}} \bar{a} \chi_{\text{ptr}}(t) * (\bar{a}^* \delta a(t) + \bar{a} \delta a^\dagger(t)) - ig_0 \bar{a} \delta q(t) - \\ & - i\bar{a} \delta\omega_{\text{tr}}(t) + \sqrt{\kappa_{\text{ex}}} \delta s_{\text{in}}(t) + \sqrt{\kappa_0} \delta s_{\text{cav}}(t) \end{aligned} \quad (\text{S24})$$

$$\begin{aligned} \Omega_m^{-1} [\delta \ddot{q}(t) + \Gamma_m \delta \dot{q}(t) + \Omega_m^2 \delta q(t)] = & -2g_0 (\bar{a} \delta a^\dagger(t) + \bar{a}^* \delta a(t)) + \\ & + \delta f_{\text{th}}(t) + \chi_{\text{pte}}(t) * (\bar{a} \delta a^\dagger(t) + \bar{a}^* \delta a(t)) \end{aligned} \quad (\text{S25})$$

with $\bar{\Delta} = \omega_1 - (\omega_c + g_0\bar{q} + \kappa_{\text{abs}}|\bar{a}|^2(\chi_{\text{ptr}}(t) * 1))$. This set of equations is best solved in the Fourier domain, yielding

$$(-i(\bar{\Delta} + \Omega) + \kappa/2) \delta a(\Omega) = -i\kappa_{\text{abs}}\bar{a}\chi_{\text{ptr}}(\Omega)(\bar{a}^*\delta a(\Omega) + \bar{a}\delta a^\dagger(\Omega)) - ig_0\bar{a}\delta q(\Omega) + \\ - i\bar{a}\delta\omega_{\text{tr}}(\Omega) + \sqrt{\kappa_{\text{ex}}}\delta s_{\text{in}}(\Omega) + \sqrt{\kappa_0}\delta s_{\text{cav}}(\Omega) \quad (\text{S26})$$

$$\frac{-\Omega^2 - i\Omega\Gamma_{\text{m}} + \Omega_{\text{m}}^2}{\Omega_{\text{m}}}\delta q(\Omega) = (-2g_0 + \chi_{\text{pte}}(\Omega))(\bar{a}\delta a^\dagger(\Omega) + \bar{a}^*\delta a(\Omega)) + \delta f_{\text{th}}(\Omega). \quad (\text{S27})$$

For simplicity, we refer to the Fourier transform of the respective functions by simply writing them with a frequency (Ω) argument. Note that $\delta a^\dagger(\Omega)$ denotes the Fourier transform of $\delta a^\dagger(t)$, equal to $[\delta a(-\Omega)]^\dagger$; and that $[\delta q(-\Omega)]^\dagger = \delta q(\Omega)$ for the Hermitian operator $\delta q(t)$.

To further simplify the problem, we approximate the response functions of the photothermal effects by a single-pole, low-pass response, assuming implicitly that the relevant temperature (gradient) distributions adjust themselves only with a certain delay to a change in the absorbed optical power. Assuming that this delay is larger than the relevant oscillation periods considered here, one can approximate

$$\chi_{\text{ptr}}(\Omega) \approx \frac{g_{\text{ptr}}}{\kappa_{\text{abs}}} \frac{\Omega_{\text{m}}}{-i\Omega} \quad (\text{S28})$$

$$\chi_{\text{pte}}(\Omega) \approx 2g_{\text{pte}} \frac{\Omega_{\text{m}}}{-i\Omega} \quad (\text{S29})$$

and finally obtains

$$(-i(\bar{\Delta} + \Omega) + \kappa/2) \delta a(\Omega) = \bar{a}g_{\text{ptr}} \frac{\Omega_{\text{m}}}{\Omega}(\bar{a}^*\delta a(\Omega) + \bar{a}\delta a^\dagger(\Omega)) - ig_0\bar{a}\delta q(\Omega) + \\ - i\bar{a}\delta\omega_{\text{tr}}(\Omega) + \sqrt{\kappa_{\text{ex}}}\delta s_{\text{in}}(\Omega) + \sqrt{\kappa_0}\delta s_{\text{cav}}(\Omega) \quad (\text{S30})$$

$$\frac{-\Omega^2 - i\Omega\Gamma_{\text{m}} + \Omega_{\text{m}}^2}{\Omega_{\text{m}}}\delta q(\Omega) = -2 \left(g_0 - ig_{\text{pte}} \frac{\Omega_{\text{m}}}{\Omega} \right) (\bar{a}\delta a^\dagger(\Omega) + \bar{a}^*\delta a(\Omega)) + \delta f_{\text{th}}(\Omega). \quad (\text{S31})$$

These equations are used to calculate the coherent response and fluctuation spectra (cf. sections 3.5, 3.6).

3.4 Homodyne detection

The optomechanical experiment is embedded into one arm of a balanced homodyne interferometer. At the initial beamsplitter, the laser field (and fluctuations in the fiber mode) are split up into a ‘local oscillator’ arm, and the arm that serves as input to the cavity:

$$s_{\text{in}} = \sqrt{1-r}s_{\text{las}} - \sqrt{r}s_{\text{bs}} \quad (\text{S32})$$

$$s_{\text{lo}} = \sqrt{r}s_{\text{las}} + \sqrt{1-r}s_{\text{bs}}, \quad (\text{S33})$$

evidently valid both in time and frequency domain. Here, we also take into account the vacuum fluctuations δs_{bs} entering the beamsplitter at the unoccupied port,

$$s_{\text{las}} = \bar{s}_{\text{las}} + \delta s_{\text{las}} \quad (\text{S34})$$

$$s_{\text{bs}} = \delta s_{\text{bs}}. \quad (\text{S35})$$

The field s_{in} drives both the mean field \bar{a} and the field fluctuations within the cavity, as described in the previous section. The intracavity field a , in turn, couples back into the single-mode fiber taper, and the usual input-output formalism gives the field s_{out} at the output of the cavity via the relation

$$s_{\text{in}} - s_{\text{out}} = \sqrt{\kappa_{\text{ex}}} a \quad (\text{S36})$$

We furthermore take into account that only a fraction η_{cryo} of the light power at the output of the cavity is measured as ‘signal’ in the homodyne detector due to optical losses, e.g. in the cryostat. For $\eta_{\text{cryo}} < 1$, we again have to account for quantum vacuum δs_{cryo} that enters the optical mode,

$$s_{\text{sig}} = \sqrt{\eta_{\text{cryo}}} s_{\text{out}} + \sqrt{1 - \eta_{\text{cryo}}} s_{\text{cryo}} \quad (\text{S37})$$

$$s_{\text{cryo}} = \delta s_{\text{cryo}}. \quad (\text{S38})$$

Finally, in the homodyne receiver, the differential signal

$$\delta h = \bar{s}_{\text{lo}} e^{+i\phi_{\text{lo}}} \delta s_{\text{sig}}^\dagger + \bar{s}_{\text{lo}}^* e^{-i\phi_{\text{lo}}} \delta s_{\text{sig}} + \bar{s}_{\text{sig}} e^{-i\phi_{\text{lo}}} \delta s_{\text{lo}}^\dagger + \bar{s}_{\text{sig}}^* e^{+i\phi_{\text{lo}}} \delta s_{\text{lo}} \quad (\text{S39})$$

is measured. The fluctuational terms δh and δq of interest can then be expressed as a linear function of the fluctuations driving the system,

$$\begin{pmatrix} \delta h \\ \delta q \end{pmatrix} = M \cdot (\delta s_{\text{las}} \quad \delta s_{\text{las}}^\dagger \quad \delta s_{\text{bs}} \quad \delta s_{\text{bs}}^\dagger \quad \delta s_{\text{cav}} \quad \delta s_{\text{cav}}^\dagger \quad \delta s_{\text{cryo}} \quad \delta s_{\text{cryo}}^\dagger \quad \delta \omega_{\text{tr}} \quad \delta f_{\text{th}})^T. \quad (\text{S40})$$

Here, the coefficients of the matrix M follow directly from the relations (S30)-(S39).

3.5 Calculation of noise covariances

We assume that all input noise terms of eq. (S40) can be described by zero-mean Gaussian noise operators whose variances are known. Representing the covariances between two noise operators x and y as a symmetrized spectrum $\bar{S}_{xy}(\Omega)$ defined according to

$$\frac{1}{2} \langle \{x(\Omega), y(\Omega')\} \rangle = 2\pi \bar{S}_{xy}(\Omega) \delta(\Omega + \Omega'), \quad (\text{S41})$$

the only non-zero covariances are characterized by the spectra

$$\bar{S}_{\delta s_{\text{las}}^\dagger \delta s_{\text{las}}}(\Omega) = \bar{S}_{\delta s_{\text{cav}}^\dagger \delta s_{\text{cav}}}(\Omega) = \bar{S}_{\delta s_{\text{bs}}^\dagger \delta s_{\text{bs}}}(\Omega) = \bar{S}_{\delta s_{\text{cryo}}^\dagger \delta s_{\text{cryo}}}(\Omega) = \frac{1}{2} \quad (\text{S42})$$

for the optical quantum noise entering the system,

$$\bar{S}_{\delta f_{\text{th}}\delta f_{\text{th}}}(\Omega) \approx 4\bar{n}_{\text{m}}\Gamma_{\text{m}} \quad (\text{S43})$$

for the thermal Langevin force, where we have assumed $\bar{n}_{\text{m}} \approx k_{\text{B}}T/\hbar\Omega_{\text{m}} \gg 1$, and

$$\bar{S}_{\delta\omega_{\text{tr}}\delta\omega_{\text{tr}}}(\Omega) = \bar{S}_{\text{trn}}(\Omega), \quad (\text{S44})$$

for the thermorefractive noise [20], whose contribution we found to be negligible in the data presented in this manuscript. By the linearity of equation (S40), it follows that the covariance matrix N_{out} of the output noise operators is then related to the input covariance matrix N_{in} by the simple expression

$$N_{\text{out}} = M(+\Omega) \cdot N_{\text{in}} \cdot M(-\Omega)^T. \quad (\text{S45})$$

3.6 Coherent dynamics of the system

In order to calculate the coherent response of the system to the probing by a phase-modulated input, eq. (S40) can be used. By assuming a sufficiently narrow detection bandwidth and/or sufficiently large phase modulation of depth $\delta\varphi$, one can set

$$\delta s_{\text{cav}}^{\dagger} \approx \delta s_{\text{cav}} \approx \delta s_{\text{bs}}^{\dagger} \approx \delta s_{\text{bs}} \approx \delta s_{\text{cryo}}^{\dagger} \approx \delta s_{\text{cryo}} \approx \delta f_{\text{th}} \approx \delta\omega_{\text{tr}} \approx 0 \quad (\text{S46})$$

$$\delta s_{\text{las}} = i\bar{s}_{\text{las}}\delta\varphi, \quad (\text{S47})$$

and calculate the frequency-dependent transfer function from a phase modulation $\delta\varphi$ to the homodyne signal δh .

This coherent response is obviously directly measured in the sideband sweeps that we routinely perform (cf. section 1.1). Moreover, by multiplication of the (complex) spectrum of the excitation pulse with this transfer function, the response of the homodyne signal in the time domain can be numerically determined via the inverse Fourier transform.

3.7 Analysis of the coherent response

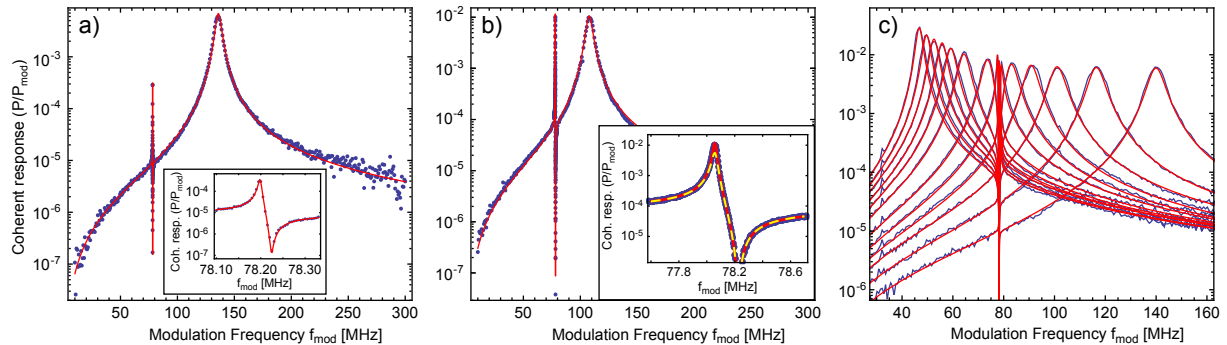
The coherent response spectra are important to accurately extract the different parameters of the optomechanical interaction as well as to calibrate the mechanical noise spectra. A typical coherent response is shown in Fig. 7a. The Lorentzian peak centered around $\Omega_{\text{mod}} = 140$ MHz results from the absorption of the upper modulation sideband by the cavity and reflects the optical response of the system. The maximum of the homodyne signal is obtained when the modulation sideband is resonant with the cavity. Hence, the center frequency and width of this peak correspond to the detuning $|\Delta|$ and the linewidth κ of the cavity, respectively. The sharp feature at $\Omega_{\text{mod}} = \Omega_{\text{m}}$ is the manifestation of Optomechanically Induced Transparency [23]; an interference effect due to the resonant excitation of the mechanical mode. For weak coupling power and/or large detuning, the

dynamics of the mechanical mode is hardly affected by the optomechanical interaction and the width of the dispersive feature is given by the mechanical linewidth Γ_m .

For larger laser power, the width of the OMIT window increases, reflecting the width of the damped mode $\Gamma_m + \Omega_c^2 \kappa / (\kappa^2 + 4(\Delta + \Omega_m)^2)$. Hence, the fit of the coherent response allows to extract the coupling rate Ω_c and the corresponding intracavity field \bar{a} . We introduce $\bar{a}_0 \equiv \bar{a} / \frac{\kappa/2}{-i\Delta + \kappa/2}$ to obtain a parameter independent of detuning. The model of eq. (S40), assuming pure radiation pressure backaction, fits the measurements well (cf. Fig. 7a). However, as can be seen in Fig. 7b, a small systematic deviation appears for high coupling power. This systematic effect is very well reproduced by the model including the photothermoelastic effect.

Finally, Figure 7c shows a series of coherent response spectra taken for decreasing laser detunings, and a laser power of 0.6 mW. The observed increase of the amplitudes for small detuning can be fitted accurately by introducing the photothermorefractive effect in the model (red lines). The parameter g_{ptr} introduced here is dependent on detuning since the thermorefractive coefficient $\frac{dn}{dT}$ depends on temperature.

For example, we have extracted from the fits to the full detuning series of Fig. 2 of the main manuscript $\Omega_m/2\pi = 78.2$ MHz, $\kappa/2\pi = 6.0$ MHz, $\bar{a}_0 = 14.2 \cdot 10^3$ (with $g_0/2\pi = 3.4$ kHz), $g_{\text{pte}}/2\pi = -122$ Hz and $g_{\text{ptr}}/2\pi = 0.32$ Hz (at the lower mechanical sideband).



Supplementary Figure 7: **Fitting the model to the coherent response.** (a) A coherent response spectrum taken with a power of 0.56 mW, at T=0.65 K. (b) Spectrum for 1.4 mW, at T=0.8 K with fits including the photothermoelastic effect (red line) and without (yellow dashed). (c) Spectra for 0.6 mW at T=0.75 K, for various detunings. The photothermorefractive effect is included in the fitted model and accounts for the increased amplitude for small detuning.

3.8 Extraction of the decoherence rate

The fits of the coherent response spectra determine all parameters characterizing the optomechanical interaction, and therefore the transduction of mechanical displacement fluctuations to optical fluctuations. The spectral shape of the noise originating from the Langevin force is thus fixed, so that the amplitude of this contribution can be fitted using the model of eq. (S45). As we fit the spectral density of the actually measured *voltage* signal, these extracted amplitudes depend on the gain of the subsequent detection chain, which is not precisely known.

This ambiguity is removed by a calibration technique [5] based on a reference phase modulation, which allows to relate noise spectra taken under arbitrarily different acquisition conditions. In this manner, we link the low-temperature noise spectra to a measurement at a higher cryostat temperature (4 K), in which a high helium gas pressure, and low optical power (~ 100 nW) ensure the thermalization of the sample, so that the Langevin force is known to an estimated accuracy of 3%. In this high-temperature measurement, a known phase modulation is applied, whose amplitude can be compared with the coherent response spectra acquired with every low-temperature measurement. Assuming that no drift occurs in the phase modulation chain, this method allows to absolutely calibrate the Langevin force—and therefore the mechanical decoherence rate—in the low-temperature measurements. Importantly, this derivation reveals possible changes of the decoherence rate both due to a changed temperature (bath occupation \bar{n}_m) and mechanical dissipation rate Γ_m .

3.9 Error analysis

We use the large number of traces acquired during a detuning sweep to estimate an error on each of the four parameters assumed to be independent of the detuning (Ω_m , κ , \bar{a}_0 , g_{pte}). This is achieved by successively letting each of these parameters vary with the detuning, while the three others are still fitted globally. The error on each parameter X is obtained by calculating the standard deviation $\Delta X = \sqrt{\langle (X - X_0)^2 \rangle}$, where X_0 is the value obtained when all four parameters are kept constant over the whole detuning range. Advantageously, this procedure reflects also systematic errors due to drifts of the experimental settings over the detuning series, and physical effects that are not captured by the model. The following uncertainties were obtained with this method for the run presented in Fig. 2 of the main manuscript: $\Omega_m/2\pi = (78.2260 \pm 0.0007)$ MHz, $\kappa/2\pi = (6.04 \pm 0.08)$ MHz, $\bar{a}_0 = (14.2 \pm 0.2) \times 10^3$, $g_{\text{pte}}/2\pi = (-122 \pm 52)$ Hz. These errors, by affecting the shape of the expected noise spectra, also translate in an error on the fitted decoherence rate and occupation. A Monte-Carlo approach is used to assess the final error on γ and \bar{n} . The fit of the noise spectrum is repeated with a set of randomly drawn parameters, assuming an independent normal distribution for each of the previous parameters. Importantly, the resulting uncertainty depends on the particular detuning

point. On the lower optomechanical sideband, the standard deviation of the results is given by $(\Delta\gamma/\gamma)_{\text{model}} = 6\%$ and $(\Delta\bar{n}/\bar{n})_{\text{model}} = 4\%$. Another source of uncertainty for these two parameters is the independent calibration of the optomechanical transduction that we estimate to be on the order of $\Delta_{\text{calib}} = 3\%$ from the scatter between calibration measurements taken at different probing power. Finally, as discussed in section 1.2, an uncertainty Δ_{GAWBS} is quadratically added to account for the possible presence of GAWBS in the optical fibers before the cavity. The total error for this example is given by

$$\frac{\Delta\gamma}{\gamma} = \sqrt{\left(\frac{\Delta\gamma}{\gamma}\right)_{\text{model}}^2 + \Delta_{\text{calib}}^2 + \Delta_{\text{GAWBS}}^2} = 10\%$$

$$\frac{\Delta\bar{n}}{\bar{n}} = \sqrt{\left(\frac{\Delta n}{n}\right)_{\text{model}}^2 + \Delta_{\text{calib}}^2 + \Delta_{\text{GAWBS}}^2} = 7\%.$$

References and Notes

- [1] Schliesser, A., Rivière, R., Anetsberger, G., Arcizet, O. & Kippenberg, T. Resolved-sideband cooling of a micromechanical oscillator. *Nature Phys.* **4**, 415–419 (2008).
- [2] Rabl, P., Genes, C., Hammerer, K. & Aspelmeyer, M. Phase-noise induced limitations in resolved-sideband cavity cooling of mechanical resonators. *Phys. Rev. A* **80**, 063819 (2009).
- [3] Diósi, L. Laser linewidth hazard in optomechanical cooling. *Phys. Rev. A* **78**, 021801 (2008).
- [4] Rocheleau, T. *et al.* Preparation and detection of a mechanical resonator near the ground state of motion. *Nature* **463**, 72–75 (2010).
- [5] Rivière, R. *et al.* Optomechanical sideband cooling of a micromechanical oscillator close to the quantum ground state. *Phys. Rev. A* **83**, 063835 (2011).
- [6] Shelby, R. M., Levenson, M. D. & Bayer, P. W. Guided acoustic-wave brillouin scattering. *Phys. Rev. B* **31**, 5244–5252 (1985).
- [7] Kippenberg, T. J., Rokhsari, H., Carmon, T., Scherer, A. & Vahala, K. J. Analysis of Radiation-Pressure Induced Mechanical Oscillation of an Optical Microcavity. *Phys. Rev. Lett.* **95**, 033901 (2005).
- [8] Anetsberger, G., Rivière, R., Schliesser, A., Arcizet, O. & Kippenberg, T. J. Ultralow-dissipation optomechanical resonators on a chip. *Nature Photon.* **2**, 627–633 (2008).

- [9] Schliesser, A. & Kippenberg, T. J. Cavity optomechanics with whispering-gallery mode optical micro-resonators. vol. 58 of *Advances In Atomic, Molecular, and Optical Physics*, 207 – 323 (Academic Press, 2010).
- [10] Gorodetsky, M., Schliesser, A., Anetsberger, G., Deleglise, S. & Kippenberg, T. J. Determination of the vacuum optomechanical coupling rate using frequency noise calibration. *Opt. Express* **18**, 23236–23246 (2010).
- [11] Enss, C. & Hunklinger, S. *Low Temperature Physics* (Springer, 2005).
- [12] Arcizet, O., Rivière, R., Schliesser, A., Anetsberger, G. & Kippenberg, T. J. Cryogenic properties of optomechanical silica microcavities. *Phys. Rev. A* **80**, 021803(R) (2009).
- [13] Nowacki, W. *Dynamic problems of thermoelasticity* (Springer, 1975).
- [14] Law, C. K. Interaction between a moving mirror and radiation pressure: A Hamiltonian formulation. *Phys. Rev. A* **51**, 2537–2541 (1995).
- [15] Fabre, C. *et al.* Quantum-noise reduction using a cavity with a movable mirror. *Phys. Rev. A* **49**, 1337–1343 (1994).
- [16] Mancini, S. & Tombesi, P. Quantum noise reduction by radiation pressure. *Phys. Rev. A* **49**, 4055–4065 (1994).
- [17] Gardiner, C. W. & Zoller, P. *Quantum Noise* (Springer, 2004).
- [18] Landau, L. D. & Lifshitz, E. M. *Statistical Physics*, vol. 5 of *Course of Theoretical Physics* (Pergamon Press, 1980), 3rd edn.
- [19] Braginsky, V. B., Gorodetsky, M. L. & Vyatchanin, S. P. Thermodynamical fluctuations and photo-thermal shot noise in gravitational wave antennae. *Phys. Lett. A* **264**, 1–10 (1999).
- [20] Gorodetsky, M. L. & Grudinin, I. S. Fundamental thermal fluctuations in microspheres. *Journal of the Optical Society of America B* **21**, 697–705 (2004).
- [21] Schliesser, A., Anetsberger, G., Rivière, R., Arcizet, O. & Kippenberg, T. J. High-sensitivity monitoring of micromechanical vibration using optical whispering gallery mode resonators. *New J. Phys.* **10**, 095015 (2008).
- [22] Anetsberger, G. *et al.* Measuring nanomechanical motion with an imprecision far below the standard quantum limit. *Phys. Rev. A* **82**, 061804 (2010).
- [23] Weis, S. *et al.* Optomechanically induced transparency. *Science* **330**, 1520–1523 (2010).